CHEMISTRY OF MATERIALS
Article

Chem. Mater. **2009,** *21,* 5375–5381 5375
DOI:10.1021/cm9013392

Neodymium Dioxide Carbonate as a Sensing Layer for Chemoresistive CO_2 Sensing

Igor Djerdj,[†,‡] Alexander Haensch,[§] Dorota Koziej,[†] Suman Pokhrel,[§] Nicolae Barsan,[§] Udo Weimar,[§] and Markus Niederberger*[,†]

[†]*Laboratory for Multifunctional Materials, Department of Materials, ETH Zurich, Wolfgang-Pauli-Strasse 10, 8093 Zurich, Switzerland,* [‡]*Ruđer Bošković Institute, Bijenička 54, 10000 Zagreb, Croatia, and* [§]*University of Tuebingen, Institute of Physical and Theoretical Chemistry, Auf der Morgenstelle 15, 72076 Tuebingen, Germany*

Received May 15, 2009. Revised Manuscript Received October 12, 2009

We report the synthesis of neodymium hydroxide nanoparticles via a nonaqueous and surfactant-free sol−gel process and their subsequent thermal transformation into neodymium dioxide carbonate, which can be applied as a sensing layer for resistive-readout CO_2 sensing. The sensors show an increase in resistance when exposed to CO_2 in both dry and humid air in the operation temperature range of 250−400 °C, with a maximum sensor signal of 4 in humid air at 350 °C in 1000 ppm CO_2. Another important feature of the sensor is the fact that exposure to water vapor leads to a pronounced decrease in resistance (opposite of the CO_2 effect), which indicates different charge-transfer mechanisms. The CO_2 gas-sensing mechanism was studied via the Operando approach, by performing direct-current (DC) resistance and diffuse reflectance infrared Fourier transform spectroscopy (DRIFTS) measurements simultaneously under operation conditions. This combination enables the correlation of any concentration changes of specific surface species with electrical effects. The correlation found between the concentration of surface-adsorbed OH and carbonate species and the electrical conductivity suggests that the reaction between CO_2 and water-related surface species is responsible for the gas-sensing effect.

Introduction

CO_2 is ubiquitous in our daily lives, and it plays an important role in health-related issues, transportation, and the environment. Therefore, CO_2 sensors are used in many applications, e.g., in agricultural and biotechnological processes, air conditioning systems, or exhaust gases.[1] In contrast to gases such as O_2, H_2, Cl_2, CO, or NO_x, which can easily be monitored by means of gas−solid interactions based on redox reactions, CO_2 is rather inert, with respect to reduction or oxidation reactions.[2] For this reason, the development of CO_2 sensors based on semiconductor gas sensor technology (i.e., the translation of CO_2 adsorption into measurable changes of electrical conductance) is a difficult and challenging task. Although CO_2 is a typical representative of an acid−base active gas,[2] which means that adsorption can occur on basic sites of selected metal oxide surfaces, sometimes leading to changes in the electron affinity, because of the redistribution of electrical charges between the surface site and the CO_2 molecule, such effects are difficult to monitor. Localized chemisorption processes do not affect the concentration of free charge carriers, and, therefore, they do not influence the electrical resistance. Consequently, commercially available state-of-the-art CO_2 sensors make use of nondispersive infrared (NDIR), electrochemical, or thermal conductivity detecting principles. The optical sensors (IR, NDIR) represent the largest group of commercially available CO_2 sensors, because CO_2 adsorbs strongly at 2349 cm^{-1},[3] and the adsorption is a function of the CO_2 partial pressure. However, this sensor technology suffers from limitations such as high costs, problems of miniaturization, and restricted lifetimes due to drift effects.[2] As a matter of fact, commercially available CO_2 sensors are characterized by a rather high complexity of the overall configuration, and there is still much room for improvement, mainly with respect to size, weight, and costs. For these reasons, several alternative approaches to low-cost and stable CO_2 gas sensors have been developed and proposed in the literature, including solid electrolyte type (potentiometric),[2,4−8] capacitive,[9−11] or field-effect-transistor[12,13] sensors. There are also some

*Author to whom correspondence should be addressed. Tel.: 41 44 633 6390. Fax: 41 44 633 1545. E-mail: Markus.Niederberger@mat.ethz.ch.

(1) Eranna, G.; Joshi, B. C.; Runthala, D. P.; Gupta, R. P. *Crit. Rev. Solid State Mater. Sci.* **2004**, *29*, 111–188.
(2) Holzinger, M.; Maier, J.; Sitte, W. *Solid State Ionics* **1997**, *94*, 217–225.
(3) Baraton, M. I. *Sens. Actuators, B* **1996**, *31*, 33–38.
(4) Gauthier, M.; Chamberland, A. *J. Electrochem. Soc.* **1977**, *124*, 1579–1583.
(5) Maier, J.; Holzinger, M.; Sitte, W. *Solid State Ionics* **1994**, *74*, 5–9.
(6) Yamazoe, N.; Miura, N. *J. Electroceram.* **1998**, *2*, 243–255.
(7) Obata, K.; Kumazawa, S.; Shimanoe, K.; Miura, N.; Yamazoe, N. *Sens. Actuators, B* **2001**, *76*, 639–643.
(8) Bobacka, J.; Ivaska, A.; Lewenstam, A. *Chem. Rev.* **2008**, *108*, 329–351.
(9) Ishihara, T.; Higuchi, M.; Takagi, T.; Ito, M.; Nishiguchi, H.; Takita, T. *J. Mater. Chem.* **1998**, *8*, 2037–2042.

Published on Web 10/29/2009

publications that describe the resistive sensors, based on a change in the electrical conductance of a semiconducting material upon exposure to CO_2 in air. Examples include SnO_2 in combination with various metals[14] or La_2O_3,[15] rare-earth metal oxide-based materials,[16] porous hydroxyapatite,[17] polyethylene glycol−inorganic salt solutions supported on ceramics,[18,19] $BaCeO_3$-based ceramics,[20] In_2Te_3,[21] LaOCl,[22] or CaO-loaded In_2O_3.[23] However, in most of these cases, the resistance/conductance changes are negligible: a change of 10%−20%, to 1000 ppm CO_2, much less than the possible influence of interfering gases (H_2O, CO, NO_2).

In this publication, we present a two-step preparation route to neodymium dioxide carbonate nanoparticles, which can be used as a chemoresistive sensing layer for CO_2 gas detection. In a first step, crystalline neodymium hydroxide nanoparticles were prepared by a nonaqueous and surfactant-free sol−gel process,[24−28] involving the reaction of neodymium isopropoxide with acetophenone. The resulting powder, screen-printed onto alumina substrates, was then thermally transformed into neodymium dioxide carbonate in the presence of CO_2. The so-achieved sensing layers showed considerable changes in electrical direct current (DC) resistance under CO_2 exposure, i.e., an increase in resistance in both dry and humid air in the operation temperature range of 250−400 °C. The recorded effects are, for a resistive CO_2 sensor, exceptionally high (a maximum sensor signal of 4 in humid air at 350 °C in 1000 ppm CO_2). Another important feature of the sensor is the fact that exposure to water vapor leads to a pronounced decrease in resistance (opposite of the CO_2 effect), which indicates different charge-transfer mechanisms.

(10) Ishihara, T.; Kometani, K.; Mizuhara, Y.; Takita, Y. *Sens. Actuators, B* **1993**, *13*, 470–472.
(11) Endres, H. E.; Hartinger, R.; Schwaiger, M.; Gmelch, G.; Roth, M. *Sens. Actuators, B* **1999**, *57*, 83–87.
(12) Star, A.; Han, T. R.; Joshi, V.; Gabriel, J. C. P.; Gruner, G. *Adv. Mater.* **2004**, *16*, 2049–2052.
(13) Shimanoe, K.; Goto, K.; Obata, K.; Nakata, S.; Sakai, G.; Yamazoe, N. *Sens. Actuators, B* **2004**, *102*, 14–19.
(14) Hoefer, U.; Kuhner, G.; Schweizer, W.; Sulz, G.; Steiner, K. *Sens. Actuators, B* **1994**, *22*, 115–119.
(15) Yoshioka, T.; Mizuno, N.; Iwamoto, M. *Chem. Lett.* **1991**, 1249–1252.
(16) Sugai, T.; Matsuzawa, T. *Sens. Actuators, B* **1993**, *13*, 480–482.
(17) Nagai, M.; Nishino, T.; Saeki, T. *Sens. Actuators* **1988**, *15*, 145–151.
(18) Egashira, M.; Shimizu, Y.; Eshita, A. *J. Electrochem. Soc.* **1988**, *135*, 2546–2547.
(19) Shimizu, Y.; Komori, K.; Egashira, M. *J. Electrochem. Soc.* **1989**, *136*, 2256–2260.
(20) Hibino, T.; Iwahara, H. *Sens. Actuators, B* **1993**, *13*, 483–485.
(21) Desai, R. R.; Lakshminarayana, D.; Patel, P. B.; Panchal, C. J. *Sens. Actuators, B* **2005**, *107*, 523–527.
(22) Marsal, A.; Dezanneau, G.; Cornet, A.; Morante, J. R. *Sens. Actuators, B* **2003**, *95*, 266–270.
(23) Prim, A.; Pellicer, E.; Rossinyol, E.; Peiro, F.; Cornet, A.; Morante, J. R. *Adv. Funct. Mater.* **2007**, *17*, 2957–2963.
(24) Niederberger, M.; Garnweitner, G. *Chem.—Eur. J.* **2006**, *12*, 7282–7302.
(25) Pinna, N.; Niederberger, M. *Angew. Chem., Int. Ed.* **2008**, *47*, 5292–5304.
(26) Djerdj, I.; Arcon, D.; Jaglicic, Z.; Niederberger, M. *J. Solid State Chem.* **2008**, *181*, 1574–1584.
(27) Mutin, P. H.; Vioux, A. *Chem. Mater.* **2009**, *21*, 582–596.
(28) Niederberger, M.; Pinna, N. *Metal Oxide Nanoparticles in Organic Solvents: Synthesis, Formation, Assembly and Application*; Springer: London, 2009.

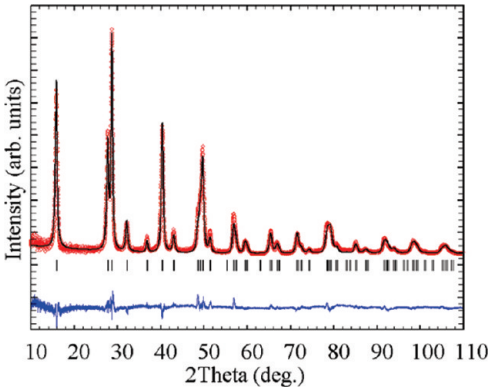

Figure 1. Observed (red circles), calculated (black line), and difference (blue line at the bottom) plots for the structure refinement of the $Nd(OH)_3$ nanoparticulate material from powder X-ray diffraction (XRD) data. The Bragg positions for $Nd(OH)_3$ are displayed by the vertical tick marks.

Results and Discussion

The as-synthesized $Nd(OH)_3$ nanoparticles were carefully characterized, with respect to phase purity, crystallinity, and morphology. Figure 1 shows a typical Rietveld refinement plot based on laboratory powder X-ray diffraction (XRD) data of $Nd(OH)_3$. All Bragg peaks can unambiguously be indexed within the space group $P6_3/m$ (176) of the hexagonal crystal system with unit-cell parameters of $a = b = 6.424(1)$ Å and $c = 3.748(2)$ Å, which agrees nicely with the literature ($a = 6.421$ Å, $c = 3.734$ Å)[29] and ICDD data ($a = 6.421$ Å, $c = 3.74$ Å, ICDD File Card No. 06-0601). The rather sharp reflections, as well as the low background, are indicative of the high crystallinity of the nanoparticles. The overall crystallite size, obtained by averaging all values in the different [*hkl*] directions, is equal to 14.3 nm, with a standard deviation (as a measure of anisotropy) of 1.7 nm only. Obviously, there is no clear preferred direction of crystal growth, although the particle morphology exhibits an anisotropic shape.

The morphology of the nanoparticles was studied by scanning electron microscopy (SEM) and transmission electron microscopy (TEM), and some representative images are shown in Figures 2a and 2b. They illustrate that the product is composed of nonuniform particles with a sligthly anisotropic rodlike shape. The sizes of the nanorods were measured on an ensemble of 100 nanorods along and perpendicular to their axes. The average length is ~27 nm, with an average diameter of ~9 nm, resulting in an aspect ratio of ~3. However, these numbers must be considered with caution, because the nanoparticles are rather agglomerated on the TEM grid. Further insight into the structure of the nanoparticles was obtained by probing the local crystallinity of a single nanorod by HRTEM imaging. Figure 2c shows a part of a $Nd(OH)_3$ nanorod, revealing lattice fringes in an arrangement that is typical for polycrystals. As already proposed by the Rietveld refinement, the individual nanocrystalline building blocks are almost isotropic, but they assemble into anisotropic structures. This observation points to a particle-mediated

(29) Morss, L. R.; Haar, C. M.; Mroczkowski, S. *J. Chem. Thermodyn.* **1989**, *21*, 1079–1083.

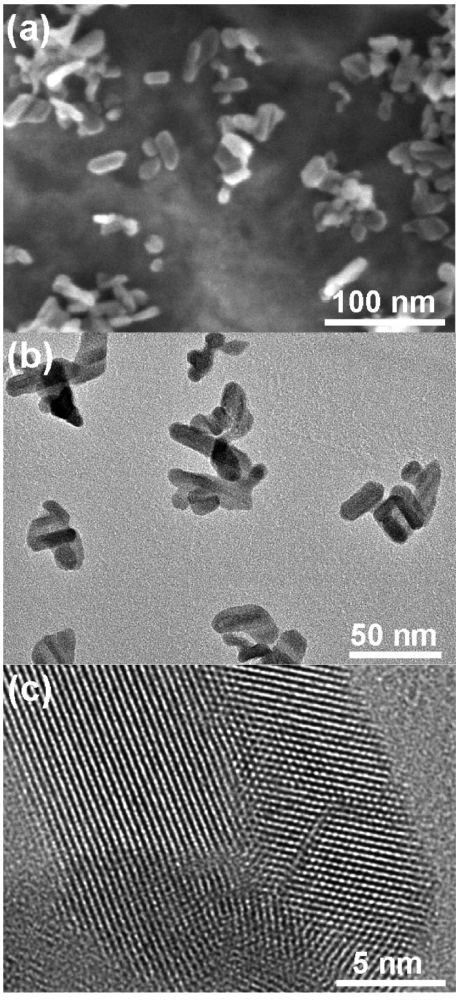

Figure 2. (a) Scanning electron microscopy (SEM) and (b) transmission electron microscopy (TEM) overview images of the as-synthesized $Nd(OH)_3$ nanorods. (c) High-resolution transmission electron microscopy (HRTEM) image of a part of a $Nd(OH)_3$ nanorod.

crystallization process.[30] However, in contrast to the oriented attachment mechanism, which is a frequently reported growth model for nanorod formation on the nanoscale,[31−33] in this case, the nanocrystals are not crystallographically oriented, with respect to each other.

The pinkish colored $Nd(OH)_3$ powder was mixed with 1,2-propanediol to form a paste, which was screen-printed on alumina substrates that were provided with interdigitated platinum electrodes for the readout of the resistance on the front side, and platinum heaters on the back side. The screen-printed sensors were dried at room temperature for 24 h, then heated in an oven at 70 °C for 4 h and finally annealed in air at 400 °C in a belt oven with multiple heating zones. At the end of the thermal treatments, the color of the layer was pale blue, and according to XRD measurements, its structure is almost amorphous. Figure 3 indicates that, within a range of

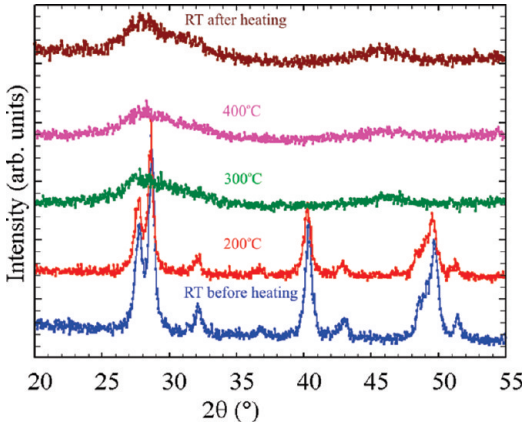

Figure 3. Temperature-dependent XRD patterns of the as-synthesized $Nd(OH)_3$ nanoparticles measured in air. Room-temperature (RT) patterns before and after the heating are also displayed.

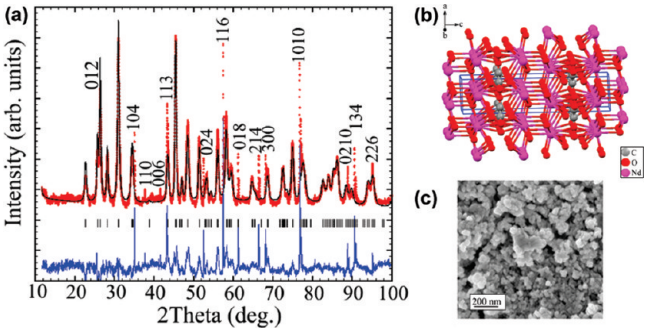

Figure 4. (a) Rietveld plot of the $Nd_2O_2CO_3$ crystal structure refinement from XRD data at room temperature. The experimental XRD pattern of the sensor device is marked in red, comprising, besides broadened lines of $Nd_2O_2CO_3$ nanoparticles, also sharp indexed lines of the substrate (α-Al_2O_3). The calculated profile is drawn as a solid black line, and the difference curve is shown in blue. Vertical tick marks correspond to the position of the Bragg reflections of $Nd_2O_2CO_3$. (b) Crystal structure of $Nd_2O_2CO_3$ slightly tilted from the view along the *b*-axis. (c) SEM image of the $Nd_2O_2CO_3$ nanoparticles as a sensing layer on the sensor substrate.

200−300 °C, a significant peak broadening occurs, pointing to a decrease in crystallinity. Surprisingly, the transformation to the crystalline $Nd_2O_2CO_3$ occurs only after exposing the heated layer to CO_2. Just heating in air is obviously not enough. It is reasonable to assume that such a low crystallinity is a prerequisite for the high reactivity of the material to be transformed into the dioxide carbonate by CO_2 gas. As a matter of fact, just a short exposure to 5000 ppm CO_2 in a background of humid air at a moderate temperature of 250 °C resulted in the complete (i.e., not only surface, but also bulk) transformation of the amorphous layer into nanocrystalline and phase-pure $Nd_2O_2CO_3$. XRD measurements of the sensing layer after the sensing tests proved the high stability of the neodymium dioxide carbonate, because no structural differences were found in the bulk phase before and after the sensing tests.

The $Nd_2O_2CO_3$ sensing layers were characterized by XRD and SEM. The XRD pattern in Rietveld plot form (Figure 4a) is rather complex and very different from that of the initial, as-synthesized $Nd(OH)_3$ nanoparticles. Two sets of reflections can be clearly distinguished. The first group consists of sharp peaks from the

(30) Niederberger, M.; Cölfen, H. *Phys. Chem. Chem. Phys.* **2006**, *8*, 3271–3287.
(31) Penn, R. L.; Banfield, J. F. *Geochim. Cosmochim. Acta* **1999**, *63*, 1549–1557.
(32) Ribeiro, C.; Vila, C.; Elias de Matos, J. M.; Bettini, J.; Longo, E.; Leite, E. R. *Chem.—Eur. J.* **2007**, *13*, 5798–5803.
(33) Zhang, Q.; Liu, S. J.; Yu, S. H. *J. Mater. Chem.* **2009**, *19*, 191–207.

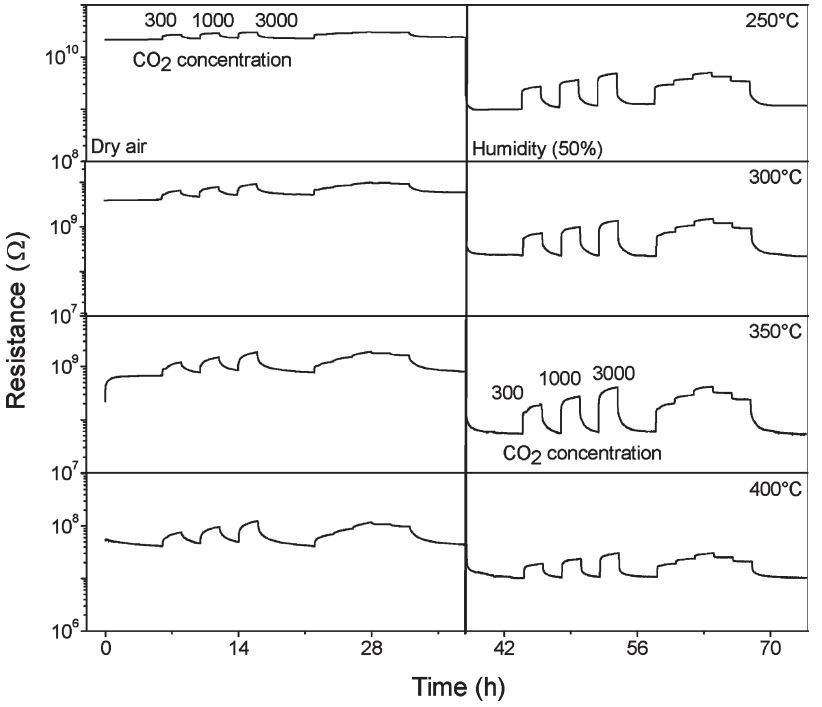

Figure 5. Gas-sensing characteristics of $Nd_2O_2CO_3$ sensors exposed to CO_2 (300, 1000, and 3000 ppm), both in the presence of dry air (left panels) and humid air (right panels). The first three exposures were performed in an on-and-off process, whereas the following three CO_2 pulses (with the same concentrations) were performed without purging with synthetic air.

α-Al_2O_3 (corundum) substrate. These reflections are denoted and indexed in Figure 4a. However, because they belong to a well-known phase and are much sharper than the others, they were not considered in the Rietveld refinement. The second family of reflections exhibits significant peak broadening and can be assigned to neodymium dioxide carbonate $Nd_2O_2CO_3$ (ICDD File Card No. 01-070-2152). This compound crystallizes in the hexagonal crystal system, space group $P6_3/mmc$, with the refined lattice parameters $a = b = 3.989\,(1)$ Å, $c = 15.650\,(1)$ Å, as deduced from the Rietveld fit ($R_{wp} = 9.9\%$) of the experimental powder XRD pattern. Reflections from the platinum electrode were not distinguishable.

The crystal structure of $Nd_2O_2CO_3$ (Figure 4b) consists of irregular NdO_8 rhombohedra, arranged in hexagonal layers along the *c*-axis with the composition Nd_2O_2. The layers are interconnected by carbonate ions. It was reported that $Nd_2O_2CO_3$ can be obtained as bulk material via decomposition of the corresponding oxalate in a stream of carbon dioxide at 500−600 °C, or via hydrothermal single-crystal growth from freshly precipitated $Nd(OH)_3$ and an aqueous solution of CO_2.[34,35] Although one could draw some analogies between the latter synthesis routes and our approach, the main difference is that we started from nanoparticulate $Nd(OH)_3$ with an average crystallite size of ~14 nm, and we also ended up with $Nd_2O_2CO_3$ nanoparticles (average crystallite size of 18 nm). These findings suggest that the presence of CO_2 and humidity mainly affect the composition, but not so much the morphology of the nanosized sensing layer (i.e., the size and shape of the nanoparticles remain practically the same throughout the entire cycle of experiments). This statement is further confirmed by SEM studies on the final sensing layers, still displaying a slightly anisotropic morphology (see Figure 4c).

The sensor tests were performed at 250, 300, 350, and 400 °C with a CO_2 exposure of 300, 1000, and 3000 ppm alternately in dry and humid air. Figure 5, which depicts the sensing performance, clearly shows that the baseline resistance is reduced by more than 1 order of magnitude in the presence of humidity in the temperature range of 250−350 °C. This effect is less pronounced when the temperature is increased to 400 °C. Also, the baseline is more stable in 50% relative humidity (RH) at all temperatures. The resistance significantly decreases as the temperature increases. The resistance at 250 °C in air ($2.2 \times 10^{10}\ \Omega$) is reduced by almost 3 orders of magnitude upon changing the temperature to 400 °C ($4.2 \times 10^{7}\ \Omega$). The same effect is observed in the presence of humidity. The CO_2 effects in dry air (left panels in Figure 5) are significantly lower in magnitude, compared to those at 50% RH (right panels) for all but the highest temperatures (also see Figure 6). In addition, the sensor signals in dry air and in humid air vary not only quantitatively (i.e., in magnitude) but also qualitatively. In dry air, even 1 h of CO_2 exposure is not long enough to reach a stable response time, which is especially visible after the stepwise increase in CO_2 concentration. Under humid conditions, the sensor response (i.e., the time required to reach 90% of the stable response) and recovery times are much shorter than the exposure time. Such an improvement of the sensing performance under humid conditions is rather unusual for a chemoresitive sensor. Typically,

(34) Sawyer, J. O.; Caro, P.; Eyring, L. *Monatsh. Chem.* **1971**, *102*, 333–354.
(35) Christensen, A. N. *Acta Chem. Scand.* **1970**, *24*, 2440–2446.

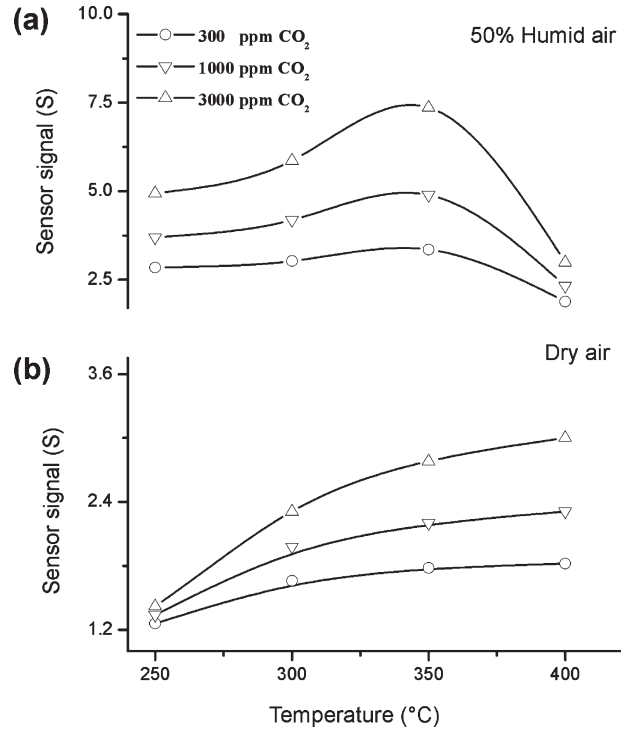

Figure 6. Sensor signals achieved in the temperature range of 250−400 °C as a function of CO_2 concentration (300, 1000, and 3000 ppm) (a) in 50% RH and (b) in dry air.

resistive metal oxide sensors for reducing gases such as CO or CH_4 suffer from cross-sensitivity to water vapors.[36] The enhanced sensor signal for CO_2 in humidity underlines the great potential of the $Nd_2O_2CO_3$-based sensors for applications under real operating conditions.

However, in humid air, the sensor signal reaches a maximum at 350 °C (see Figure 6a); no such effect is observed in the presence of dry air (see Figure 6b).

The CO_2 gas sensing mechanism was explored by applying the Operando investigation approach,[36,37] i.e., the spectroscopic and phenomenological measurements were performed under operation conditions and on functional sensors. DC resistance and diffuse reflectance infrared Fourier transform spectroscopy (DRIFTS) measurements were simultaneously performed during CO_2 exposure in dry and humid air as backgrounds. Such a combination of techniques enables the correlation of any concentration changes of specific surface species with electrical effects, identifying the species that are responsible for the sensor effect (i.e., for the change in resistance). Because water vapor and CO_2 gas both strongly affect the electrical behavior (variation of oxygen gas concentration as background does not produce any significant changes in resistance, data not shown), two spectral regions must be studied thoroughly. The carbonate (symmetric and asymmetric streching) bands generally observed in the range of 1200−1700 cm^{-1} and the ν_{OCO} peaks at ~1050 cm^{-1} and 860 cm^{-1} are expected to vary due to the CO_2 adsorption. The region above 2500 cm^{-1}, showing the stretching vibrations of differently bound hydroxyl groups and adsorbed water, should reflect the concentration of these water-related species, which are influenced by the humidity level in the environment.

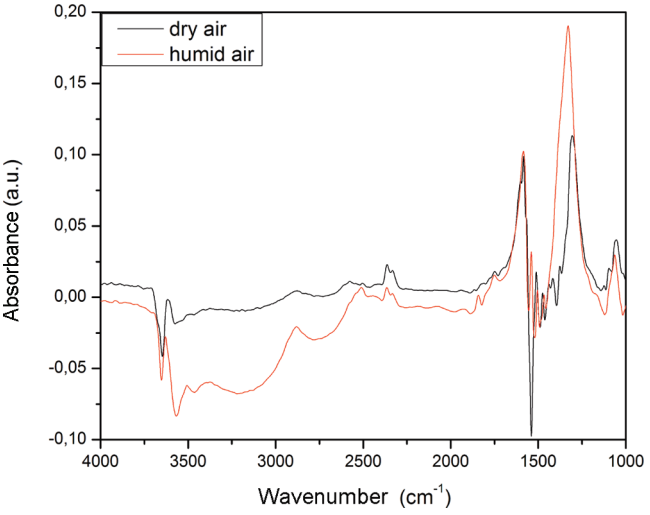

Figure 7. DRIFT difference spectra of the $Nd_2O_2CO_3$ sensor during exposure to 300 ppm CO_2 under dry and humid conditions at 300 °C.

The DRIFT difference spectra during exposure to a concentration of 300 ppm CO_2 under dry and humid conditions (50% RH at 25 °C) are shown in Figure 7. The reference spectra were recorded before the CO_2 exposure in dry and humid air, respectively (for an explanation of the methodology, see the Experimental Section and refs 38 and 39). In both cases, the decrease of the concentration of all water-related species (multiple negative bands) and an increase of the concentration of different carbonates (multiple positive bands in the range of 1700−1200 cm^{-1}) are visible. Noticeable in the spectrum are the negative bands at ~1400−1550 cm^{-1}, indicating that the carbonate bands are disturbed. Because of almost-total absorption, interpretation of any changes in this range is not reliable. The observation that CO_2 exposure leads to a decrease in the concentration of water-related surface species, as well as an increase of surface carbonate bands, makes us propose that the reaction between CO_2 and water-related species is responsible for the gas-sensing effect. Note that there is a quantitative correlation between the spectroscopic and electrical results (i.e., higher changes in the surface species concentrations are mirrored by higher sensor effects), and this observation gives further evidence for the proposed model involving a reaction between water-related species and CO_2 molecules. In humid air, for example, one expects to find more water-related species at the surface of the material, and, consequently, the interaction is stronger (the decrease in the integrated area of all water-related species is ~5 times higher than that observed under dry conditions, which is consistent with the higher sensor effects (from 2 to 6)). On the other hand, water exposure not only increases the

(36) Barsan, N.; Koziej, D.; Weimar, U. *Sens. Actuators, B* **2007**, *121*, 18–35.
(37) Gurlo, A.; Riedel, R. *Angew. Chem., Int. Ed.* **2007**, *46*, 3826–3848.
(38) Harbeck, S.; Szatvanyi, A.; Barsan, N.; Weimar, U.; Hoffmann, V. *Thin Solid Films* **2003**, *436*, 76–83.
(39) Koziej, D.; Barsan, N.; Hoffmann, V.; Szuber, J.; Weimar, U. *Sens. Actuators, B* **2005**, *108*, 75–83.

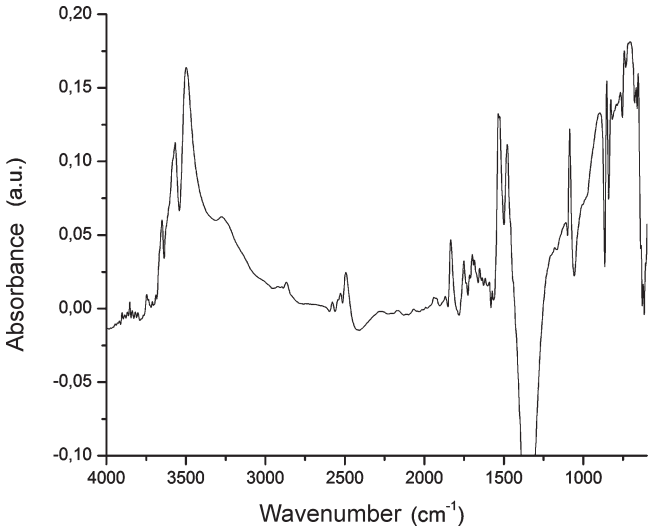

Figure 8. DRIFT difference spectrum between sensors operating under dry and humid conditions at 300 °C.

concentration of the surface hydroxyl groups, but also decreases the amount of carbonates and thus produces the opposite effect of CO_2, in terms of resistance changes. The DRIFT difference spectrum in Figure 8 between dry and 50% relative humidity shows a considerable production of different hydroxyls (adsorption bands above 3500 cm^{-1}) and a consumption of the carbonate groups (absorption band centered at ~1342 cm^{-1}). The changes in the spectrum are different from those recorded in Figure 7, indicating that CO_2 and water do not simply compete for the same adsorption sites. Quantitatively, the changes are consistent with the higher effect of humidity on the resistance of the sensor, suggesting that the changes in the electrical resistance are correlated with concentration changes of surface hydroxyl groups and/or carbonates. At this moment, it is not yet clear whether both surface species (hydroxyl and carbonate groups) have an electrical effect, or if just one species is responsible for the change in resistance and the other one acts as a chemical partner in the reaction.

Conclusions

Neodymium hydroxide nanoparticles, prepared from neodymium isopropoxide and acetophenone, can easily be transformed to neodymium dioxide carbonate, and this material is a promising candidate for resistive CO_2 sensors. $Nd_2O_2CO_3$ exhibits a good sensor signal for CO_2 in dry air as well as humid air. As a matter of fact, the best sensing performance was obtained in humid air, which represents the real operating conditions. The results are remarkable, from a scientific point of view as well as from a technological point of view. On the one hand, the change in resistance of $Nd_2O_2CO_3$ upon exposure to CO_2 opens up an interesting question about the sensing mechanism; on the other hand, the composition of $Nd_2O_2CO_3$ points to the possibility that other metal carbonates also might be applied as a sensing layer in resistive CO_2 sensors. Although many difficulties (e.g., improvement of response and recovery times, decrease of baseline resistance, cross sensitivity toward other gases) must be overcome before such a material can be applied in a real CO_2 sensor, the results are encouraging and hopefully intensify research efforts in this direction.

Experimental Section

Materials. Neodymium isopropoxide (99.8%) was obtained from Sigma−Aldrich, and acetophenone (99%) was obtained from Acros Organics. The chemicals were used as-received.

Synthesis. The synthesis procedure was conducted in a glovebox (O_2 and H_2O < 0.1 ppm), and was as follows: 965.3 mg of $Nd(OiPr)_3$ (3 mmol) was added to 20 mL of acetophenone. The reaction mixture was transferred into a Teflon cup of 45 mL inner volume, slid into a steel autoclave (Parr acid digestion bomb), and carefully sealed. The autoclave was taken out of the glovebox and heated in a furnace at 200 °C for 2 days. The resulting suspension was centrifuged to separate the precipitate from the mother liquid. Excess organic impurities were removed by repeated washing cycles in 10 mL of high-grade purity ethanol (2×) and in chloroform (1×) and finally dried in air at 60 °C, yielding a fine pinkish powder.

Fabrication of Sensors. The pinkish colored $Nd(OH)_3$ powder was mixed with 1,2-propanediol to form a paste, which was screen-printed on alumina substrates that were provided with interdigitated platinum electrodes for the readout of the resistance on the front side, and platinum heaters on the back side. The substrates were purchased from CeramTec AG. The screen-printed sensors were dried at room temperature for 24 h, then heated in an oven at 70 °C for 4 h and finally annealed in air at 400 °C in a belt oven (Centrotherm) with multiple heating zones. At the end of the thermal treatment, the layer had a pale-blue color and was almost amorphous. The final sensing material ($Nd_2O_2CO_3$) was obtained when the sensor was exposed to CO_2 under real sensor operating conditions (250 °C and under a flow of CO_2 in air).

Gas-Sensing Measurements. The sensor tests were performed with individual sensors placed in a homemade Teflon test chamber and operated at 250, 300, 350, and 400 °C. The gas mixtures were adjusted by a gas-mixing system. Prior to the first exposure, the sensors were conditioned in dry air for 6 h, followed by exposing different concentrations of CO_2. At each operation temperature, the sensors were exposed to 300, 1000, and 3000 ppm CO_2 alternately in dry and humid air (50% RH at 25 °C). The sensing properties were assessed through the sensor signal S, which is defined as the resistance ratio (R_{air}/R_{gas}, where R_{gas} and R_{air} denote the resistances of the sensors either in the presence or absence of analyte gas, respectively). The sensor resistance was measured with a Keithley Model EMM 617 system.

Characterization. Phase purity, crystallinity, and morphology of the as-synthesized nanoparticulate material was thoroughly characterized by various techniques such as X-ray diffraction (XRD), scanning electron microscopy (SEM), transmission electron microscopy (TEM), and high-resolution transmission electron microscopy (HRTEM). XRD data were collected in reflection mode on a X'Pert PRO MPD diffractometer equipped with an X'Celerator linear detector, using Cu Kα radiation and a step size of 0.01°. Structural refinement from these data was performed using the Rietveld program FULLPROF. The refinement was performed by varying the background, zero-point error, peak profile parameters, scale factor, unit-cell parameters, atomic coordinates, and the atomic thermal parameters. Temperature-dependent XRD measurements were conducted

from room temperature up to 400 °C in an air atmosphere using a high-temperature Anton Paar chamber (Model HTK 1200). The diffuse reflectance infrared Fourier transform spectroscopy (DRIFTS) measurements were performed with a Bruker Vertex 80v vacuum Fourier transform infrared (FT-IR) spectrometer equipped with a Harrick Praying Mantis DRIFTS unit and a homemade sensor chamber. The vacuum in the interferometer compartment was stable at 1.62 mbar during all measurements. For interferogram recording, a DTGS detector was used. Every single-channel spectrum was calculated from the co-addition of 900 interferometer scans at a resolution of 4 cm^{-1}. For the spectroscopy on the working sensor, the sensor was exposed for 1 h to the background gas, followed by another 1 h exposure to the testing gas and then another hour to the background gas. Four spectra were recorded per hour. The resulting absorbance spectra were calculated using the last spectrum under background gas exposure as the reference spectrum. TEM and HRTEM characterization was performed using a JEOL Model 2200FS TEM/STEM system that was operated at 200 kV and equipped with an in-column Omega energy filter. The samples for TEM characterization were prepared in such a way that one drop of the dispersion of the as-synthesized powder in ethanol, sonicated for ~5 min, was deposited onto a copper grid that was covered by an amorphous carbon film.

Acknowledgment. Financial support by ETH Zürich, the Deutsche Forschungsgemeinschaft (WE 3662/4-1), and the Alexander von Humboldt foundation is gratefully acknowledged. We thank Marta D. Rossell for recording the TEM and HRTEM images, and we are thankful for the support of the Electron Microscopy Center at EMPA Dübendorf, Switzerland.